

www.acsami.org Research Article

Photocurrent in Metal-Halide Perovskite/Organic Semiconductor Heterostructures: Impact of Microstructure on Charge Generation Efficiency

Colin Tyznik, James Lee, Jeni Sorli, Xiaojie Liu, Emma K. Holland, Cynthia S. Day, John E. Anthony, Yueh-Lin Loo, Z. Valy Vardeny, and Oana D. Jurchescu*



Cite This: https://dx.doi.org/10.1021/acsami.0c21992



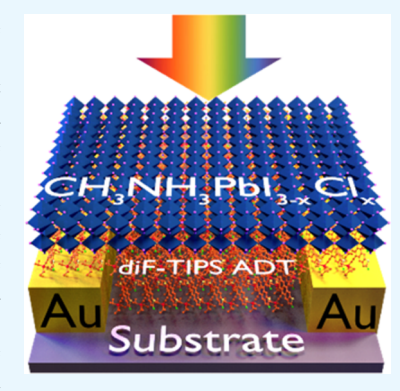
ACCESS

III Metrics & More

Article Recommendations

Supporting Information

ABSTRACT: Hybrid organic—inorganic metal-halide perovskites have emerged as versatile materials for enabling low-cost, mechanically flexible optoelectronic applications. The progress has been commendable; however, technological breakthroughs have outgrown the basic understanding of processes occurring in bulk and at device interfaces. Here, we investigated the photocurrent at perovskite/organic semiconductor interfaces in relation to the microstructure of electronically active layers. We found that the photocurrent response is significantly enhanced in the bilayer structure as a result of a more efficient dissociation of the photogenerated excitons and trions in the perovskite layer. The increase in the grain size within the organic semiconductor layer results in reduced trapping and further enhances the photocurrent by extending the photocarriers' lifetime. The photodetector responsivity and detectivity have improved by 1 order of magnitude in the optimized samples, reaching values of $6.1 \pm 1.1 \text{ A W}^{-1}$, and $1.5 \times 10^{11} \pm 4.7 \times 10^{10}$ Jones, respectively, and the current—voltage hysteresis has been eliminated. Our results highlight the importance of fine-tuning film



microstructure in reducing the loss processes in thin-film optoelectronics based on metal-halide semiconductors and provide a powerful interfacial design method to consistently achieve high-performance photodetectors.

KEYWORDS: photocurrent, perovskite, organic semiconductors, photodetector, recombination, charge transport

■ INTRODUCTION

Photodetectors represent key components in optoelectronic devices serving technologies such as image sensors, security and surveillance, biomedical monitoring, optical communications, environment and process monitoring. Large-area, flexible photodetectors expand their application space toward incorporation into conformal medical applications, rollable displays, and wearable electronics.^{1–4} The emergence of hybrid organic-inorganic metal-halide perovskites (MPH) has opened new avenues in photodetection research by simultaneously offering high absorption coefficients, long charge carrier diffusion lengths, and tunable band gaps, along with the opportunity for low-cost processability. 5-7 Indeed, metalhalide perovskites have been incorporated in various photodetector structures, including photodiodes and phototransistors, both as photoactive and transport layers.^{8–11} Perovskite photodetectors (PPDs) exploit the band gap tunability, high charge carrier mobilities and the low complexity processing using scalable, low-cost fabrication methods. 9,12-14 Both broad-band and narrow-band detectors with high performance over a wide range of wavelengths have been demonstrated in polycrystalline films, single crystals, and nanowires. 12,15-17 Integration of perovskites with other semiconductors, such as organic semiconductors (OSC), transition metal dichalcogenides, or graphene, provides yet another opportunity for performance enhancement by tuning the built-in potential at the heterointerface in multilayer devices, which, in turn, can effectively suppress the carrier recombination. The progress has been remarkable; however, minimizing the losses during the photocarriers extraction and collection processes remains a challenge due to the severe impact of grain boundaries and intragrain defects on charge transport and trap-related nonradiative recombination. The proportion of the process of the severe impact of grain boundaries and intragrain defects on charge transport and trap-related nonradiative recombination.

In this work, we report on the photoresponse of heterojunctions that consist of prototype metal-halide perovskite/organic semiconductor thin films, in relation to their microstructure. The functional bilayer structure combines the high absorption efficiency of the perovskite with the efficient charge separation achieved at the interface with the organic semiconductor as a result of a staggered band gap alignment, to yield significantly higher photocurrent compared to single-layer

Received: December 11, 2020 Accepted: February 9, 2021



devices. We fine-tune the microstructure of the organic semiconductor layer by modifying the substrate chemistry and investigate the dynamics of photocarrier generation and transport using electrical and structural characterization. We found that in heterostructures with optimized microstructure, the current—voltage hysteresis is suppressed and the photoresponse sensitivity is substantially enhanced, leading to one order of magnitude improvement in the responsivity and detectivity. Concurrently, a faster temporal response is achieved due to more efficient charge separation and transfer at the heterointerface.

■ RESULTS AND DISCUSSION

The electrical properties of heterojunctions that comprise of bilayers of methylammonium lead triiodide perovskite $(CH_3NH_3PbI_{3-x}Cl_x$ or MAPI) and 2,8-difluoro-6,13-bis-(triisopropylsilylethynyl) anthradithiophene (diF-TIPS ADT) were measured in a lateral architecture, with planar bottom contacts, as shown schematically in Figure 1a. The structures

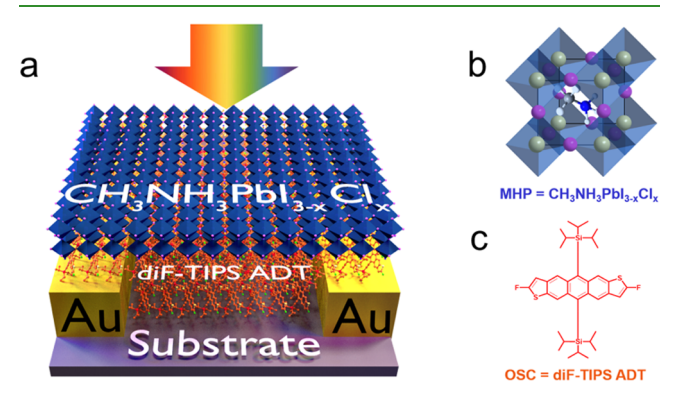


Figure 1. (a) Schematic representation of the device architecture that shows the bottom gold contacts (yellow), as well as the OSC (red) and MHP (blue) layers. (b) Crystal structure of $MAPbI_{3-x}Cl_x$, where the yellow spheres represent the Pb^{2+} cations, the purple spheres are the halide anions (I⁻/Cl⁻), and the organic cation $CH_3NH_3^+$ sits in the interstices. (c) Molecular structure of the diF-TIPS ADT organic semiconductor molecule.

of the two materials are included in Figure 1b,c, respectively. We will refer to the metal-halide perovskite layer as MHP, and to the organic semiconductor layer as OSC. In this simple design, light is absorbed through the MHP layer, the photoexcitations migrate toward the interface with the OSC, dissociate at this interface, and the resulting photocarriers are transported through the OSC layer to be collected at the contacts. Two types of bilayer samples have been investigated, along with the controls consisting of MHP and OSC single layers, which have been fabricated and tested under the same conditions. For type I device, the OSC was deposited directly over the SiO₂ substrates with prepatterned Au electrodes. This deposition procedure resulted in uniform films that consist of micron-size grains, which can be seen in Figure 2a,b, where we include the scanning electron microscopy (SEM) and polarized optical images, respectively, acquired on a typical OSC film. The average grain area for these films was 3.0 ± 1.8 μ m²; a histogram showing the distribution of grain areas is included in Figure 2c. We will refer to these samples as OSC SG (small grain) samples. For type II device, the OSC was deposited on substrates with a lower surface energy that results from the chemical modification of Au with pentafluoro

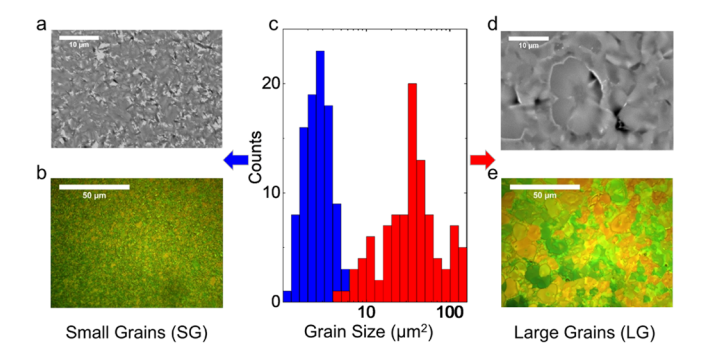
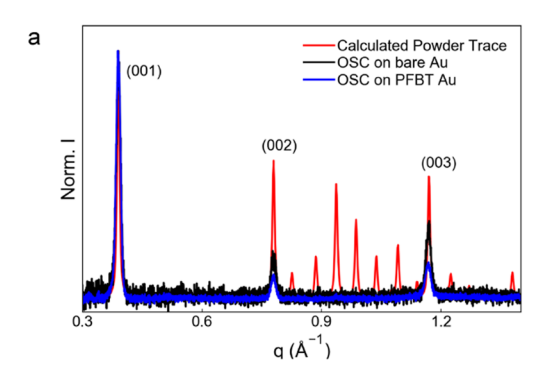


Figure 2. (a) SEM micrograph obtained on a SG OSC film; (b) polarized optical micrograph of a SG OSC film; (c) histogram of SG (blue) and LG (red) OSC grain-size distributions; (d) SEM micrograph obtained on a LG OSC film; and (e) polarized optical micrograph of an LG OSC film.

benzene thiol (PFBT) self-assembled monolayer (SAM). Upon SAM treatment of the electrode, the water contact angle increases from 37.1 to 82.5°, which corresponds to a decrease in surface energy from ~50 to ~35 mJ/mm², as shown in our previous work.²⁵ The average grain size for the OSC layer in device type II was measured to be 44.3 ± 34.1 μ m², see Figure 2c; this is an order of magnitude increase compared to the OSC in type I device; we will refer to these films as OSC LG (large grain). Corresponding SEM images and optical micrographs of such OSC films are provided in Figure 2d,e, respectively. The larger grains obtained in LG films are a consequence of reducing the affinity between the OSC molecules in the solution and the Au substrate upon lowering the surface energy with PFBT treatment—a typical outcome for films that crystallize via a nucleation and growth mechanism.²⁶ We expect a more efficient charge transport in samples consisting of LG as a result of a reduced density of high-resistivity grain boundaries. However, we acknowledge that the nature and respective orientations of the grain boundaries determine their influence on the optoelectronic properties of the films. ^{25,27,28} This effect will also be enhanced by a more efficient charge injection/collection occurring in the LG films due to the reduction in the injection barrier by approx. 0.3-0.5 eV upon PBFT treatment of the Au electrodes. 25,29 We also characterized the perovskite layer deposited over the SG and LG OSC, respectively; in Figure S1, we show the SEM images performed on the cross sections of the films. While a small variation is observed in the lateral grain size, the thickness is nominally the same. In addition, no statistically relevant differences have been noted with respect to the grain size within the perovskite layer.

To evaluate if surface functionalization influences molecular packing within the OSC layer, we performed grazing incidence X-ray diffraction (XRD) on SG and LG OSC films. In our previous work, we have shown that the interaction strength between the OSC and the chemically tailored surface governs the rate of crystallization and the final microstructure of the OSC film, ³⁰ and the molecular orientation with respect to the substrate can be "edge-on" (i.e., with the molecular backbone perpendicular to the plane of the substrate), "face-on" (i.e., with the molecular backbone parallel to the plane of the substrate), or a combination of grains consisting of each orientation and that coalesce where the growth fronts meet. ^{31,32} Figure 3a compares the calculated powder diffraction pattern from the known single crystal of diF-TIPS



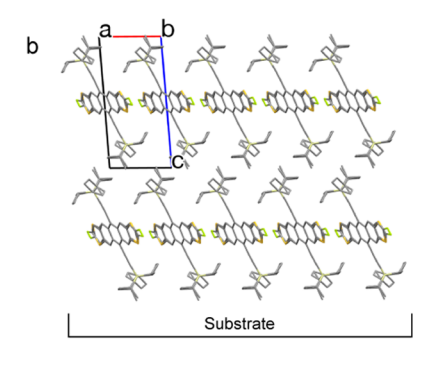


Figure 3. (a) Calculated powder diffraction pattern from a single crystal of OSC (red), XRD patterns of OSC on bare Au (black), and PFBT Au (blue) showing crystal orientation. (b) Illustration of small-molecule edge-on orientation with respect to the substrate plane. Hydrogen atoms are hidden for clarity.

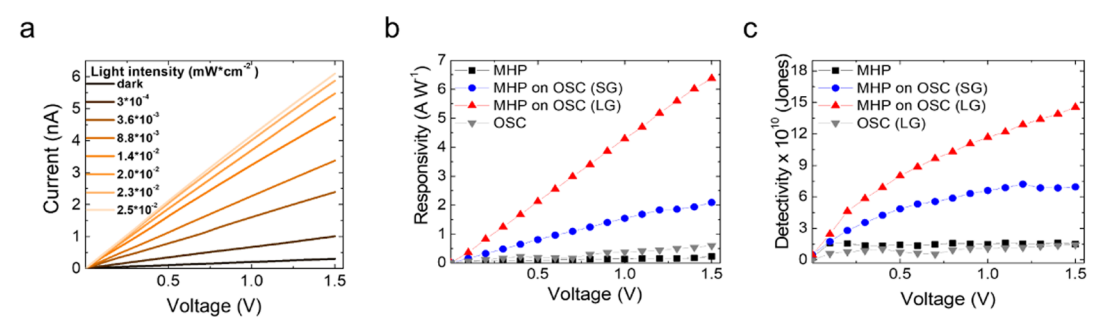


Figure 4. (a) Typical photocurrent response as a function of light power density and applied voltage in an MHP on the LG OSC bilayer sample. (b) Device responsivity of various photodetector types measured as a function of voltage at a constant light power density of 3×10^{-4} mW cm⁻². (c) Device detectivity measured as a function of applied voltage at a constant light power density of 3×10^{-4} mW cm⁻².

ADT with the high-resolution XRD traces acquired on both types of films.³³ We observe that diF-TIPS ADT in both SG and LG films adopt the same crystal structure as the bulk single crystal. Furthermore, diF-TIPS ADT is preferentially oriented edge-on relative to the substrate, as evidenced by the (001) family of reflections in the out-of-plane diffraction traces of the SG and LG films. While surface treatment impacts grain size, it appears not to alter the crystal structure or the preferential orientation adopted by diF-TIPS ADT in these OSC films. We also analyzed the structure of the MHP layer when deposited over the SG and LG type films, respectively. We found that the film structure is similar to that where the MHP solution is deposited directly onto the substrate (Figure S2). In all sample types, the perovskite layer crystallizes in the tetragonal phase and adopts a preferential [110] orientation.³⁴ These measurements confirm that the composition and structure of the perovskite film are preserved in all samples and it is independent of the substrate over which it is deposited.

The photoresponse of the single layer and heterostructures based on MHP/OSC bilayers was evaluated by recording the current—voltage (I-V) characteristics in the dark, and under illumination with visible white light (spectrum shown in Figure S3). In Figure 4a, we show the photocurrent (PC) response for a device based on an MHP/LG OSC bilayer with electrode separation $L=100~\mu \mathrm{m}$, for the light power density varying between 0 (dark) and $2.5\times10^{-2}~\mathrm{mW~cm^{-2}}$. The photocurrent depends linearly on the applied voltage and increases with the light power density. These dependencies are typical for Ohmic response and monomolecular photocarrier recombination kinetics. Similar measurements were taken on all device types with the aim to directly compare the bilayer and single-

layer devices. Based on these measurements, we evaluated the responsivity (R) and detectivity (D*) from the I-V curves; the results are shown in Figure 4b,c, respectively. It can be seen that in the bilayer devices both R and D^* surpass the values obtained in measurements performed on devices based on single layers and that the photoresponse in MHP/OSC (LG) surpasses all other structures. The responsivity values in neat MHP and OSC films are comparable with those reported previously, with $R = 0.13 \pm 0.02 \text{ Å W}^{-1}$ in MHP and $R = 0.2 \pm 0.02 \text{ Å}$ 0.1 A W⁻¹ in OSC at an applied bias $V = 1.5 \text{ V.}^{35}$ The responsivity increased by over one order of magnitude in devices based on the bilayer with SG OSC ($R = 1.9 \pm 0.2$ A W⁻¹) and by almost 50 times in devices based on the bilayers with LG OSC ($R = 6.1 \pm 1.1 \text{ A W}^{-1}$). Similarly, D^* was enhanced by over 6 times in bilayers with SG OSC ($D^* = 7.1$ \times 10¹⁰ \pm 2.5 \times 10⁹ Jones) and 14 times in bilayers with LG OSC ($D^* = 1.5 \times 10^{11} \pm 4.7 \times 10^{10}$ Jones), compared to the neat MHP case $(D^* = 1.1 \times 10^{10} \pm 2.7 \times 10^9 \text{ Jones}).$

To understand the mechanism of charge separation and transport across the interface of the MHP/OSC junction and explain our experimental observations, we first focus on the comparison between devices based on single-layer films (MHP and OSC, respectively) and MHP/OSC SG bilayers. In the OSC single-layer photodetectors, light absorption leads to the formation of excitons, which, in the presence of the external electric field, dissociate generating free charges that are collected at the electrodes as photocurrent. In the MHP devices, few excitons exist at room temperature under the illumination intensity regime investigated here because the exciton binding energy is smaller than the thermal energy, $k_{\rm B}T$ = 25 meV. 36,37 However, it is possible that some photo-

generated electron—hole pairs are bound to another charge (electron or hole) originating either from defects, impurities, surface states, or simply another photogenerated charge to form trions (or "charged excitons," Figure 5a). 38,39 Coulombic

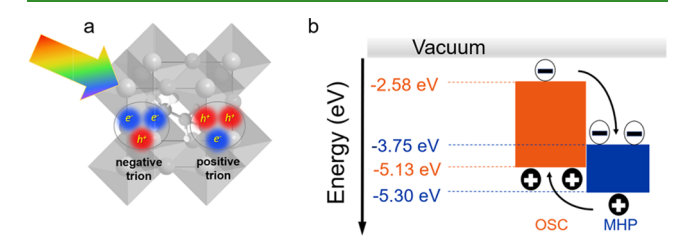


Figure 5. (a) Schematic illustration of trion formation in MHP upon optical excitation. (b) Energy level diagrams for the diF-TIPS ADT/MAPbI $_{3-x}$ Cl $_x$ bilayer photodetectors that form a Type II heterojunction.

interactions between the charge carriers within the trions give rise to "excitonic-like effects," but the binding energy is stronger compared to that of the exciton. Under an applied bias, the photogenerated trions, along with the few existing excitons, may dissociate to yield free electrons and holes. One strategy to enhance the dissociation rate is to create heterojunctions that consist of two layers of different electron affinity and/or ionization potentials. $^{40-42}$

Figure 5b shows the energy band diagram of the MHP/OSC heterojunction when the semiconductors are brought in contact.^{33,43} The staggered (Type II) band gap alignment enables efficient charge separation following photogeneration of excitons and trions. The photoexcitations migrate toward the interface with the organic semiconductor, where they separate with low recombination losses due to the built-in potential there. As a result, the charge carrier nonradiative recombination processes are suppressed and the hole and electron lifetimes are consequently extended.⁴⁴ We do not exclude, however, that some of the neutral photoexcitations dissociate already in the bulk of the perovskite layer, and free charges are spontaneously generated during this process.⁴⁵ In this case, the presence of the heterojunction does not contribute to the charge separation, but it enables selective charge collection based on the energy level alignment. Comparing the photocurrent response in the two types of heterostructures, it is clear that the LG OSC films provide a more effective platform for charge separation and transport. Given that (i) the perovskite layer is nominally identical in all

samples, implying that the charge carrier photogeneration process is similar, and (ii) the molecular orientations within the MHP and OSC layers do not change either (Figures 3 and S2), we believe that the differences in the photocurrent response stem from the variance in charge transport within the organic semiconductor, which is a direct consequence of tuning the grain size. Structural defects and impurities residing at the grain boundaries generate electronic traps, which facilitate trap-assisted recombination, a process that is less prevalent in the heterointerfaces with LG OSC. 46 Here, the large crystalline grains result in a lower trap density, 46 as confirmed by the higher hole mobility obtained using organic field-effect transistor (OFET) measurements ($\mu = 4.7 \times 10^{-2}$ cm² V⁻¹ s⁻¹ compared to $\mu = 3.3 \times 10^{-3}$ cm² V⁻¹ s⁻¹ in SG films, see Figure S4).⁴⁷ The lower defect density and faster charge transport within the OSC layer extend the photocarriers' lifetime, which, in turn, yields PC enhancement. The reduced grain boundary density was also found to eliminate the current-voltage hysteresis (Figure S5) by suppressing the most effective channels for ion migration at the heterointerface. 48 We do not exclude, however, the possibility of binding/ interaction between dif-TIPS ADT and perovskite layers, a process that can also influence the carrier dynamics at the interface. Nevertheless, the similarity in charge carrier mobility in single OSC layer and MHP/OSC bilayer devices suggests that no significant coupling between the two layers occurs in our samples.

Since most of the PC measurements were performed using a light source having a broad spectrum, it is desirable to measure the photocurrent action (or excitation) spectra (EXPC) of the various devices. The EXPC measurements were performed using a Tungsten-Halogen incandescent lamp for excitation having a broad spectrum ranging from 400 nm to 3 μ m. The excitation light was dispersed by a monochromator having 2 nm spectral resolution, and the excitation wavelength was scanned from 500 to 900 nm. The light beam was directed onto a planar device having two gold electrodes 100 μ m apart. The EXPC spectra of three devices, namely a bare MHP layer, MHP/OSC bilayers on SG OSC, and MHP/OSC bilayers on LG OSC are shown in Figure 6a-c, respectively. As can be seen, all three EXPC spectra show an onset at the MHP optical gap ~780 nm; there is a flat region from 780 to 600 nm, followed by a gradual increase from 600 to 500 nm. The increase at short wavelengths coincides with the onset of a second absorption band known to exist in MAPI (see Figure S6). This shows that the optical density (OD) of the MHP

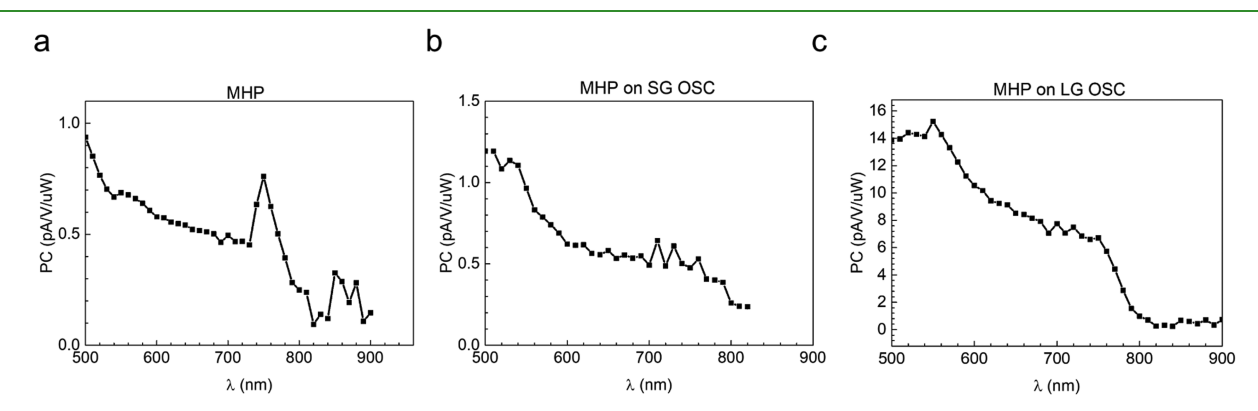


Figure 6. PC action spectra or the EXPC of photodetector based on (a) MHP single layer; (b) MHP on the SG OSC bilayer; and (c) MHP on the LG OSC bilayer.

layer was sufficiently small between 600 and 800 nm, so that the PC increase in the spectral range between 500 and 600 nm is due to a parallel increase in the MHP OD. The EXPC spectrum of the MHP single-layer device shows a pronounced band at the exciton spectral range; this confirms that the perovskite film has excellent properties. The most important observation here is the order of magnitude increase in the EXPC value for the device based on MHP/LG OSC (Figure 6c), in agreement with the measurements based on the broadband excitation described above. This result certifies that the more efficient PC obtained in the MHP/LG OSC bilayer is genuine.

The temporal response of the photocurrent for the four types of photodetectors was also investigated. The on/off switching behavior during multiple cycles recorded at a light excitation intensity of 2.5×10^{-2} mW cm⁻² and an applied voltage of 1.5 V is shown in Figure 7.

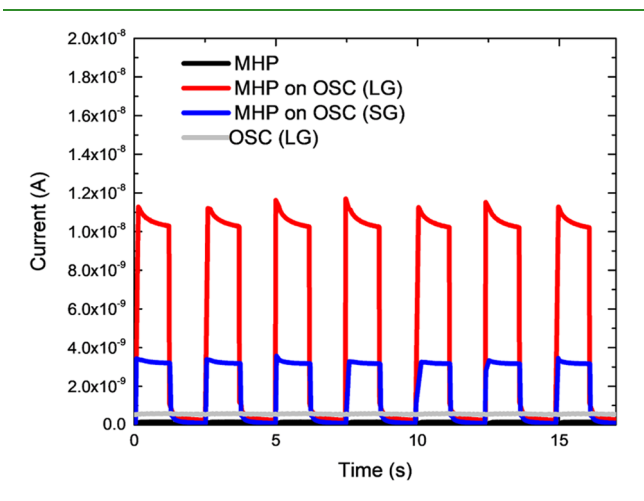


Figure 7. Transient photocurrent response for the four photodetector structures investigated here.

The calculated rise and decay times averaged over the entire length of the measurement are included in Table 1. The

Table 1. t_{rise} and t_{decay} Values of Different Photodetectors

detector material(s)	$t_{ m rise}~({ m ms})$	$t_{ m decay}~({ m ms})$
MHP	60.4 ± 1.1	330.9 ± 1.6
MHP on LG OSC	68.9 ± 1.7	76.2 ± 0.4
MHP on SG OSC	57.3 ± 1.2	16.2 ± 0.2
LG OSC	N/A	N/A

response speed of the perovskite-only device is on par with state-of-art perovskite photodetectors. Whereas the rise times are not affected by our interface engineering, the decay time is significantly reduced as a result of more efficient photoexcitation dissociation and charge transfer at the heterointerface. We note, however, that these values are inferior to those achieved in other optimized photodetector interfaces, such as perovskite/graphene, perovskite/ CdS, or perovskite/ WS_2 .

CONCLUSIONS

In summary, we found that the photocurrent response is greatly enhanced at the metal-halide perovskite/organic semiconductor interfaces and highly dependent on the organic

semiconductor film morphology. The photoconductors exhibit a responsivity of $6.1 \pm 1.1~\mathrm{A~W}^{-1}$ and detectivity of 1.5×10^{11} \pm 4.7 \times 10¹⁰ Jones in heterostructures based on organic semiconductor films with large grains. Since the morphology of the perovskite layer is similar in all devices, and the organic molecules adopt the known crystal structure and are preferentially oriented edge-on with respect to the substrate in all samples, we conclude that the observed performance improvement does not originate from differences in the interfacial coupling, but rather from a reduction in charge trapping at the grain boundaries within the organic semiconductor layer, which extends the photocarriers' lifetime. These results highlight the importance of device design and microstructure optimization in enhancing photoconductor device performance by minimizing recombination losses. A bilayer device consisting of perovskite and organic semiconductor single crystals would provide the most pristine structure, with a low trap density, and most efficient photocurrent response. Since such devices cannot be realistically incorporated in technologically relevant applications, film morphology control to enhance the grain size is imperative to improve the figures of merit of perovskite/organic semiconductor bilayer photodetectors.

MATERIALS AND METHODS

Photodetector Fabrication. Sample fabrication started from SiO₂ substrates, which were cleaned sequentially via submersion in acetone at 85 °C, submersion in isopropyl alcohol 85 °C, and a UVozone treatment for 10 min. After the UV-ozone treatment, the substrates were rinsed with deionized water (DI) and dried with a nitrogen stream, then baked for 5 min at 155 °C. These substrates were loaded into a Kurt Lesker Spectros system with a base pressure of at least 10⁻⁷ Torr. Rectangular electrodes were patterned using shadow masks and deposited via successive evaporation of 5 nm Ti and 75 nm Au. Devices were constructed using 400 μ m width electrodes at 100 μ m separation. These substrates with electrodes were cleaned following the procedure described above. To fabricate LG OSC films, an additional step was performed, where the contacts were immersed in a solution of 2,3,4,5,6-pentafluorothiophenol (PFBT) (97%, Aldrich, 12 µL) in room-temperature ethanol (3 mL) for 30 min. The semiconductor was deposited during the next step. For perovskite-only devices, the perovskite precursor solution was fabricated using PbI₂ (99.999% trace metal basis, Aldrich), PbCl₂ (99.999% trace metal basis, Aldrich), and CH3NH3I (98%, Aldrich) at a 3:0.9:0.3 (MAI/PbCl₂/PbI₂) molar ratio in a N,N-dimethylformamide (anhydrous, 99.8%, Aldrich). The solution was stirred at 80 °C for at least 12 h in a nitrogen glovebox and then deposited via spincoating at 3000 rpm for 45 s. The obtained film was heated for 90 min at 115 °C to inside a nitrogen glovebox. For OSC-only devices, a 1.5 wt % solution of diF-TIPS ADT in room-temperature chlorobenzene was deposited via spin-coating at 1000 rpm for 80 s in a nitrogen atmosphere and annealed in vacuum at room temperature for at least 6 h to remove residual solvent. The bilayer devices were obtained by depositing the perovskite precursor solution over the OSC film following the same procedures as described for the case of perovskiteonly devices.

Photodetector Electrical Characterization. The performance of photodetectors was studied by measuring the current–voltage characteristics in dark and under illumination, using an Agilent 4155C Parameter Analyzer. The electromagnetic radiation was provided by a Thorlabs MBB1F1 broad-band light-emitting diode (LED). The irradiance power was adjusted from 3×10^{-4} to 2.5×10^{-2} mW cm⁻². All measurements were performed under nitrogen and at room temperature in a Lake Shore Cryotronics TTPX cryogenic probe station. The soft nature of the films allowed easy access to the bottom electrodes using the probe tips. At least 20 devices originating from

five or more different samples of each type have been measured and included in the analysis.

Organic Semiconductor Microstructure Characterization. The SEM micrographs were obtained using a Zeiss Gemini 300 field emission scanning electron microscope (FE-SEM). The electron acceleration voltage was 3 kV. The micrographs of the organic film were obtained with an Olympus B061 optical microscope using a polarizer. OFET devices were fabricated in a bottom-gate, bottom-contact configuration, with a SiO_2 dielectric, measured under nitrogen and characterized using standard procedures. High-resolution XRD traces were collected on a Bruker D8 Discover diffractometer using a Cu K α radiation source (λ = 1.54 Å). The step size used for the collection was 0.004°.

Perovskite Structure Characterization. To evaluate the structure of the perovskite film, XRD traces were collected on all sample types using a Bruker D2 Phase diffractometer using a Cu K α radiation source (λ = 1.54 Å). The step size used for the collection was 0.014°.

Photocurrent Action Spectra. The different photodetectors were subjected to cw illumination from a Tungsten/Halogen lamp of which beam was dispersed via a 1/4 m monochromator (Jarel-Ash) with 2 nm spectral resolution. For obtaining the PC action spectrum, we normalized the measured photocurrent excitation spectrum by the light intensity spectrum obtained by a power meter.

ASSOCIATED CONTENT

Supporting Information

The Supporting Information is available free of charge at https://pubs.acs.org/doi/10.1021/acsami.0c21992.

Cross-sectional SEM images taken on the perovskite film (Figure S1); XRD patterns of the perovskite (MHP) film (Figure S2); emission spectrum of Thorlabs MBB1F1 LED (Figure S3); transfer curves obtained on diF-TIPS ADT OFET devices (Figure S4); *I–V* plots of photodetectors (Figure S5); absorption spectrum (Figure S6); and a description of photodetector characterization (PDF)

AUTHOR INFORMATION

Corresponding Author

Oana D. Jurchescu — Department of Physics and Center for Functional Materials, Wake Forest University, Winston-Salem, North Carolina 27109, United States; oorcid.org/0000-0003-2204-2909; Email: jurchescu@wfu.edu

Authors

- Colin Tyznik Department of Physics and Center for Functional Materials, Wake Forest University, Winston-Salem, North Carolina 27109, United States
- James Lee Department of Physics and Center for Functional Materials, Wake Forest University, Winston-Salem, North Carolina 27109, United States
- Jeni Sorli Department of Chemical and Biological Engineering and Andlinger Center for Energy and the Environment, Princeton University, Princeton, New Jersey 08544, United States
- Xiaojie Liu Department of Physics, University of Utah, Salt Lake City, Utah 84112, United States
- Emma K. Holland Department of Chemistry and Center for Applied Energy Research, University of Kentucky, Lexington, Kentucky 40506, United States
- Cynthia S. Day Center for Functional Materials and Department of Chemistry, Wake Forest University, Winston-Salem, North Carolina 27109, United States

- John E. Anthony Department of Chemistry and Center for Applied Energy Research, University of Kentucky, Lexington, Kentucky 40506, United States; Ocid.org/0000-0002-8972-1888
- Yueh-Lin Loo Department of Chemical and Biological Engineering and Andlinger Center for Energy and the Environment, Princeton University, Princeton, New Jersey 08544, United States; Occid.org/0000-0002-4284-0847
- Z. Valy Vardeny Department of Physics, University of Utah, Salt Lake City, Utah 84112, United States; orcid.org/ 0000-0002-2298-398X

Complete contact information is available at: https://pubs.acs.org/10.1021/acsami.0c21992

Notes

The authors declare no competing financial interest.

ACKNOWLEDGMENTS

We thank Prof. Keith Bonin for help with the photocurrent measurements. O.D.J. and C.T. acknowledge National Science Foundation (NSF) funding under awards ECCS-1608095 and DMR DMREF 1627925. X.L. and Z.V.V. acknowledge funding from the DOE, Office of Science, Grant DESC0014579. J.S. and Y.-L.L. acknowledge NSF funding under awards CMMI-1824674, DMR-1627453, and DMR-1420541; the latter of which originates from NSF's MRSEC program that supports the Princeton Center for Complex Materials. J.E.A. thanks NSF DMR DMREF 1627428 for funding, while EKH was supported by the NSF under Cooperative Agreement No. 1849213.

REFERENCES

- (1) Liu, Y.; Pharr, M.; Salvatore, G. A. Lab-on-Skin: A Review of Flexible and Stretchable Electronics for Wearable Health Monitoring. *ACS Nano* **2017**, *11*, 9614–9635.
- (2) Chow, P. C. Y.; Someya, T. Organic Photodetectors for Next-Generation Wearable Electronics. *Adv. Mater.* **2020**, 32, No. 1902045.
- (3) Khan, Y.; Ostfeld, A. E.; Lochner, C. M.; Pierre, A.; Arias, A. C. Monitoring of Vital Signs with Flexible and Wearable Medical Devices. *Adv. Mater.* **2016**, *28*, 4373–4395.
- (4) Trung, T. Q.; Lee, N. E. Flexible and Stretchable Physical Sensor Integrated Platforms for Wearable Human-Activity Monitoringand Personal Healthcare. *Adv. Mater.* **2016**, *28*, 4338–4372.
- (5) Goetz, K. P.; Taylor, A. D.; Paulus, F.; Vaynzof, Y. Shining Light on the Photoluminescence Properties of Metal Halide Perovskites. *Adv. Funct. Mater.* **2020**, *30*, No. 1910004.
- (6) Rong, Y.; Hu, Y.; Mei, A.; Tan, H.; Saidaminov, M. I.; Seok, S. Il.; McGehee, M. D.; Sargent, E. H.; Han, H. Challenges for Commercializing Perovskite Solar Cells. *Science* **2018**, *361*, No. eaat8235.
- (7) Grancini, G.; Nazeeruddin, M. K. Dimensional Tailoring of Hybrid Perovskites for Photovoltaics. *Nat. Rev. Mater.* **2019**, *4*, 4–22.
- (8) Luo, L. B.; Wu, G. A.; Gao, Y.; Liang, L.; Xie, C.; Zhang, Z. X.; Tong, X. W.; Wang, T.; Liang, F. X. A Highly Sensitive Perovskite/Organic Semiconductor Heterojunction Phototransistor and Its Device Optimization Utilizing the Selective Electron Trapping Effect. *Adv. Opt. Mater* **2019**, *7*, No. 1900272.
- (9) Xie, C.; Liu, C.-K.; Loi, H.-K.; Yan, F. Perovskite-Based Phototransistors and Hybrid Photodetectors. *Adv. Funct. Mater.* **2020**, 30, No. 1903907.
- (10) Zhang, M.; Zhang, F.; Wang, Y.; Zhu, L.; Hu, Y.; Lou, Z.; Hou, Y.; Teng, F. High-Performance Photodiode-Type Photodetectors Based on Polycrystalline Formamidinium Lead Iodide Perovskite Thin Films. *Sci. Rep.* **2018**, *8*, No. 11157.

- (11) Lin, Y.-H.; Huang, W.; Pattanasattayavong, P.; Lin, J.; Li, R.; Sakai, N.; Panidi, J.; Hong, M. J.; Ma, C.; Wei, N.; Wehbe, N.; Fei, Z.; Heeney, M.; Labram, J. G.; Anthopoulos, T. D.; Snaith, H. J. Deciphering Photocarrier Dynamics for Tuneable High-Performance Perovskite-Organic Semiconductor Heterojunction Phototransistors. *Nat. Commun.* **2019**, *10*, No. 4475.
- (12) Dou, L.; Yang, Y. M.; You, J.; Hong, Z.; Chang, W.-H. H.; Li, G.; Yang, Y. Solution-Processed Hybrid Perovskite Photodetectors with High Detectivity. *Nat. Commun.* **2014**, *5*, No. 5404.
- (13) Razza, S.; Castro-Hermosa, S.; Di Carlo, A.; Brown, T. M. Research Update: Large-Area Deposition, Coating, Printing, and Processing Techniques for the Upscaling of Perovskite Solar Cell Technology. *APL Mater.* **2016**, 4, No. 091508.
- (14) Tyznik, C.; Lamport, Z. A.; Sorli, J.; Becker-Koch, D.; Vaynzof, Y.; Loo, Y.-L.; Jurchescu, O. D. Laser Printed Metal Halide Perovskites. *J. Phys. Mater.* **2020**, *3*, No. 034010.
- (15) Li, F.; Ma, C.; Wang, H.; Hu, W.; Yu, W.; Sheikh, A. D.; Wu, T. Ambipolar Solution-Processed Hybrid Perovskite Phototransistors. *Nat. Commun.* **2015**, *6*, No. 8238.
- (16) Fang, Y.; Dong, Q.; Shao, Y.; Yuan, Y.; Huang, J. Highly Narrowband Perovskite Single-Crystal Photodetectors Enabled by Surface-Charge Recombination. *Nat. Photonics* **2015**, *9*, 679–686.
- (17) Miao, J.; Zhang, F. Recent Progress on Highly Sensitive Perovskite Photodetectors. J. Mater. Chem. C 2019, 7, 1741–1791.
- (18) Chen, S.; Teng, C.; Zhang, M.; Li, Y.; Xie, D.; Shi, G. A Flexible UV—Vis—NIR Photodetector Based on a Perovskite/Conjugated-Polymer Composite. *Adv. Mater.* **2016**, 28, 5969—5974.
- (19) Ma, C.; Shi, Y.; Hu, W.; Chiu, M. H.; Liu, Z.; Bera, A.; Li, F.; Wang, H.; Li, L. J.; Wu, T. Heterostructured WS2/CH3NH3PbI3-Photoconductors with Suppressed Dark Current and Enhanced Photodetectivity. *Adv. Mater.* **2016**, *28*, 3683–3689.
- (20) Chen, Z.; Kang, Z.; Rao, C.; Cheng, Y.; Liu, N.; Zhang, Z.; Li, L.; Gao, Y. Improving Performance of Hybrid Graphene–Perovskite Photodetector by a Scratch Channel. *Adv. Electron. Mater.* **2019**, *5*, No. 1900168.
- (21) Castro-Méndez, A. F.; Hidalgo, J.; Correa-Baena, J. The Role of Grain Boundaries in Perovskite Solar Cells. *Adv. Energy Mater.* **2019**, 9. No. 1901489.
- (22) de Quilettes, D. W.; Vorpahl, S. M.; Stranks, S. D.; Nagaoka, H.; Eperon, G. E.; Ziffer, M. E.; Snaith, H. J.; Ginger, D. S. Impact of Microstructure on Local Carrier Lifetime in Perovskite Solar Cells. *Science* 2015, 348, 683–686.
- (23) Grancini, G.; Srimath Kandada, A. R.; Frost, J. M.; Barker, A. J.; De Bastiani, M.; Gandini, M.; Marras, S.; Lanzani, G.; Walsh, A.; Petrozza, A. Role of Microstructure in the Electron-Hole Interaction of Hybrid Lead Halide Perovskites. *Nat. Photonics* **2015**, *9*, 695–701.
- (24) Zeidell, A. M.; Tyznik, C.; Jennings, L.; Zhang, C.; Lee, H.; Guthold, M.; Vardeny, Z. V.; Jurchescu, O. D. Enhanced Charge Transport in Hybrid Perovskite Field-Effect Transistors via Microstructure Control. *Adv. Electron. Mater.* **2018**, *4*, No. 1800316.
- (25) Mei, Y.; Fogel, D.; Chen, J.; Ward, J. W.; Payne, M. M.; Anthony, J. E.; Jurchescu, O. D. Interface Engineering to Enhance Charge Injection and Transport in Solution-Deposited Organic Transistors. *Org. Electron.* **2017**, *50*, 100–105.
- (26) Lee, S. Š.; Muralidharan, S.; Woll, A. R.; Loth, M. A.; Li, Z.; Anthony, J. E.; Haataja, M.; Loo, Y.-L. Understanding Heterogeneous Nucleation in Binary, Solution-Processed, Organic Semiconductor Thin Films. *Chem. Mater.* **2012**, *24*, 2920–2928.
- (27) Rivnay, J.; Jimison, L. H.; Northrup, J. E.; Toney, M. F.; Noriega, R.; Lu, S.; Marks, T. J.; Facchetti, A.; Salleo, A. Large Modulation of Carrier Transport by Grain-Boundary Molecular Packing and Microstructure in Organic Thin Films. *Nat. Mater.* **2009**, *8*, 952–958.
- (28) Lee, S. S.; Mativetsky, J. M.; Loth, M. A.; Anthony, J. E.; Loo, Y.-L. Quantifying Resistances across Nanoscale Low- and High-Angle Interspherulite Boundaries in Solution-Processed Organic Semiconductor Thin Films. *ACS Nano* **2012**, *6*, 9879–9886.
- (29) Kim, C.-H.; Hlaing, H.; Hong, J.-A.; Kim, J.-H.; Park, Y.; Payne, M. M.; Anthony, J. E.; Bonnassieux, Y.; Horowitz, G.; Kymissis, I.

- Decoupling the Effects of Self-Assembled Monolayers on Gold, Silver, and Copper Organic Transistor Contacts. *Adv. Mater. Interfaces* **2015**, 2, No. 1400384.
- (30) Lee, S. S.; Tang, S. B.; Smilgies, D.-M.; Woll, A. R.; Loth, M. A.; Mativetsky, J. M.; Anthony, J. E.; Loo, Y.-L. Guiding Crystallization around Bends and Sharp Corners. *Adv. Mater.* **2012**, 24, 2692–2698.
- (31) Ward, J. W.; Li, R.; Obaid, A.; Payne, M. M.; Smilgies, D.; Anthony, J. E.; Amassian, A.; Jurchescu, O. D. Rational Design of Organic Semiconductors for Texture Control and Self-Patterning on Halogenated Surfaces. *Adv. Funct. Mater.* **2014**, 24, 5052–5058.
- (32) Ward, J. W.; Loth, M. A.; Kline, R. J.; Coll, M.; Ocal, C.; Anthony, J. E.; Jurchescu, O. D. Tailored Interfaces for Self-Patterning Organic Thin-Film Transistors. *J. Mater. Chem.* **2012**, 22, 19047.
- (33) Subramanian, S.; Park, S. K.; Parkin, S. R.; Podzorov, V.; Jackson, T. N.; Anthony, J. E. Chromophore Fluorination Enhances Crystallization and Stability of Soluble Anthradithiophene Semiconductors. *J. Am. Chem. Soc.* **2008**, *130*, 2706–2707.
- (34) Khlyabich, P. P.; Loo, Y.-L. Crystalline Intermediates and Their Transformation Kinetics during the Formation of Methylammonium Lead Halide Perovskite Thin Films. *Chem. Mater.* **2016**, *28*, 9041–9048
- (35) Lian, Z.; Yan, Q.; Lv, Q.; Wang, Y.; Liu, L.; Zhang, L.; Pan, S.; Li, Q.; Wang, L.; Sun, J.-L. High-Performance Planar-Type Photodetector on (100) Facet of MAPbI 3 Single Crystal. Sci. Rep. 2015, S, No. 16563.
- (36) Chen, X.; Lu, H.; Yang, Y.; Beard, M. C. Excitonic Effects in Methylammonium Lead Halide Perovskites. *J. Phys. Chem. Lett.* **2018**, *9*, 2595–2603.
- (37) Baranowski, M.; Plochocka, P. Excitons in Metal-Halide Perovskites. Adv. Energy Mater. 2020, 10, No. 1903659.
- (38) Kanemitsu, Y. Trion Dynamics in Lead Halide Perovskite Nanocrystals. *J. Chem. Phys.* **2019**, *151*, No. 170902.
- (39) Yarita, N.; Aharen, T.; Tahara, H.; Saruyama, M.; Kawawaki, T.; Sato, R.; Teranishi, T.; Kanemitsu, Y. Observation of Positive and Negative Trions in Organic-Inorganic Hybrid Perovskite Nanocrystals. *Phys. Rev. Mater.* **2018**, *2*, No. 116003.
- (40) Chen, Y.; Chu, Y.; Wu, X.; Ou-Yang, W.; Huang, J. High-Performance Inorganic Perovskite Quantum Dot-Organic Semiconductor Hybrid Phototransistors. *Adv. Mater.* **2017**, 29, No. 1704062.
- (41) Li, X.; Yu, D.; Chen, J.; Wang, Y.; Cao, F.; Wei, Y.; Wu, Y.; Wang, L.; Zhu, Y.; Sun, Z.; Ji, J.; Shen, Y.; Sun, H.; Zeng, H. Constructing Fast Carrier Tracks into Flexible Perovskite Photodetectors to Greatly Improve Responsivity. ACS Nano 2017, 11, 2015–2023.
- (42) Li, Z.; Li, H.; Jiang, K.; Ding, D.; Li, J.; Ma, C.; Jiang, S.; Wang, Y.; Anthopoulos, T. D.; Shi, Y. Self-Powered Perovskite/CdS Heterostructure Photodetectors. ACS Appl. Mater. Interfaces 2019, 11, 40204–40213.
- (43) Abrusci, A.; Stranks, S. D.; Docampo, P.; Yip, H. L.; Jen, A. K. Y.; Snaith, H. J. High-Performance Perovskite-Polymer Hybrid Solar Cells via Electronic Coupling with Fullerene Monolayers. *Nano Lett.* **2013**, *13*, 3124–3128.
- (44) Li, Z.; Li, J.; Ding, D.; Yao, H.; Liu, L.; Gong, X.; Tian, B.; Li, H.; Su, C.; Shi, Y. Direct Observation of Perovskite Photodetector Performance Enhancement by Atomically Thin Interface Engineering. ACS Appl. Mater. Interfaces 2018, 10, 36493—36504.
- (45) deQuilettes, D. W.; Frohna, K.; Emin, D.; Kirchartz, T.; Bulovic, V.; Ginger, D. S.; Stranks, S. D. Charge-Carrier Recombination in Halide Perovskites. *Chem. Rev.* **2019**, *119*, 11007–11019
- (46) Haneef, H. F.; Zeidell, A. M.; Jurchescu, O. D. Charge Carrier Traps in Organic Semiconductors: A Review on the Underlying Physics and Impact on Electronic Devices. *J. Mater. Chem. C* **2020**, *8*, 759–787.
- (47) Lamport, Z. A.; Haneef, H. F.; Anand, S.; Waldrip, M.; Jurchescu, O. D. Tutorial: Organic Field-Effect Transistors: Materials, Structure and Operation. *J. Appl. Phys.* **2018**, *124*, No. 071101.

- (48) Shao, Y.; Fang, Y.; Li, T.; Wang, Q.; Dong, Q.; Deng, Y.; Yuan, Y.; Wei, H.; Wang, M.; Gruverman, A.; Shield, J.; Huang, J. Grain Boundary Dominated Ion Migration in Polycrystalline Organic—Inorganic Halide Perovskite Films. *Energy Environ. Sci.* **2016**, *9*, 1752–1759.
- (49) Yi, X.; Ren, Z.; Chen, N.; Li, C.; Zhong, X.; Yang, S.; Wang, J. TiO2 Nanocrystal/Perovskite Bilayer for High-Performance Photodetectors. *Adv. Electron. Mater.* **2017**, *3*, No. 1700251.
- (50) Lee, Y.; Kwon, J.; Hwang, E.; Ra, C.-H.; Yoo, W. J.; Ahn, J.-H.; Park, J. H.; Cho, J. H. High-Performance Perovskite-Graphene Hybrid Photodetector. *Adv. Mater.* **2015**, *27*, 41–46.